Surface Science xxx (2014) xxx–xxx

Contents lists available at ScienceDirect

Surface Science

journal homepage: www.elsevier.com/locate/susc

The templated growth of a chiral transition metal chalcogenide

M.O. King [a,b,*], I.M. McLeod [c], D. Hesp [c], V.R. Dhanak [c], A. Tadich [d], L. Thomsen [d], B.C.C. Cowie [d], D.A. MacLaren [b,**], M. Kadodwala [a,**]

[a] School of Chemistry, University of Glasgow, Glasgow G12 8QQ, UK
[b] SUPA, School of Physics and Astronomy, University of Glasgow, Glasgow G12 8QQ, UK
[c] Department of Physics, University of Liverpool, Liverpool L69 3BX, UK
[d] Australian Synchrotron, 800 Blackburn Road, Clayton, Victoria 3168, Australia

ARTICLE INFO

Article history:
Received 1 November 2013
Accepted 5 February 2014
Available online xxxx

Keywords:
Chiral
Inorganic materials
Topological insulators

ABSTRACT

We demonstrate that an intrinsically chiral, high Miller index surface of an achiral metal can be used to template the enantioselective growth of chiral transition metal chalcogenide films. Specifically, Cu(643)^R can be used as a template for the enantioselective growth of a chiral copper telluride alloy surface. Beyond a critical alloy thickness the chiral influence of the Cu(643)^R surface diminishes and an achiral surface forms. Our work demonstrates a new method of producing chiral transition metal chalcogenide surfaces, with potential applications in the study of structurally chiral topological insulators.

1. Introduction

Inorganic chiral surfaces play important roles in a number of fields ranging from asymmetric catalysis [1] to speculations on the origins of life [2] and, more recently, the electronic properties of topological insulators [3]. Some naturally occurring minerals, such as quartz, have an intrinsically chiral crystallography that leads to asymmetries in any exposed surface. Chiral interfaces can also be created from achiral crystals by interaction with a chiral ligand via etching [4], electrodeposition [5] or simply via the production of ordered arrays with oblique unit cells [6,7]. Alternatively, a chiral surface can be produced from an achiral metal by exposing low-symmetry, high Miller index surfaces [8] whose kink sites can display enantioselective molecular adsorption [9], desorption and surface chemistry [10–20]. Somewhat surprisingly, there are very few examples of heteroepitaxial growth on such chiral surfaces, despite their technological potential. $SrTiO_3$(621) and Pt(321) have both been used as templating substrates for metal thin film growth, with the adsorption of Pt and Cu in the case of $SrTiO_3$(621) [20–23] and Au, Ag and Bi in the case of Pt(321) [16]. In each system, there is a general preference for adatoms to occupy the chiral kink sites in the early stages of growth, presumably driven by their higher co-ordination. In contrast, here we consider a more complex epitaxial system that has the potential for surface alloy formation. We demonstrate that chiral, high Miller index surface planes of a substrate can act as a template for the growth of nanoscale transition metal chalcogenide films with chiral structures.

The substrate used in this study is Cu(643)^R, which can be considered to be miscut from a (111) surface, the miscut giving rise to a regular array of (110) kinks and (100) steps, as illustrated in Fig. 1. The chirality of this surface stems from the orientation of kink sites. McFadden et al. [9] first attempted to describe the handedness of chiral surfaces in terms of steps of unequal length; this was later developed by Attard et al. [19], who generalised the Cahn–Ingold–Prelog priority rules [24] with regard to the {hkl} sites surrounding the chiral kink site. In the latter scheme, the handedness of a surface can be assigned depending on the order of rotation from low to higher-index microfacets about a kink site. For example, the clockwise orientation of (100) steps → (110) kinks → (111) terraces illustrated in Fig. 1 is assigned as the R enantiomer. A more rigorous framework for the description of surface chirality has subsequently been developed by Jenkins and Pratt [8] although it is not used here.

Experimental observations demonstrate that in reality the Cu(643)^R surface has significant deviations from its ideal termination, which is driven towards higher-coordinated, lower surface energy structures by the relatively high mobility of Cu adatoms at room temperature. Density functional theory calculations [25], Monte Carlo simulations [26] and scanning tunnelling microscopy (STM) [27] have shown that the surface undergoes thermal roughening. The result is an inhomogeneous distribution of steps and a larger proportion of (111) terraces, but with kinks of a single handedness that retain the overall chirality imposed by the macroscopic miscut angle [25,26]. This drive towards structures that minimise surface energy can be enhanced by deposition of an overlayer, as has often been observed on achiral, vicinal

* Correspondence to: M.O. King, AWE plc, Aldermaston, Reading, Berkshire, RG7 4PR, UK.
** Corresponding authors.

http://dx.doi.org/10.1016/j.susc.2014.02.008

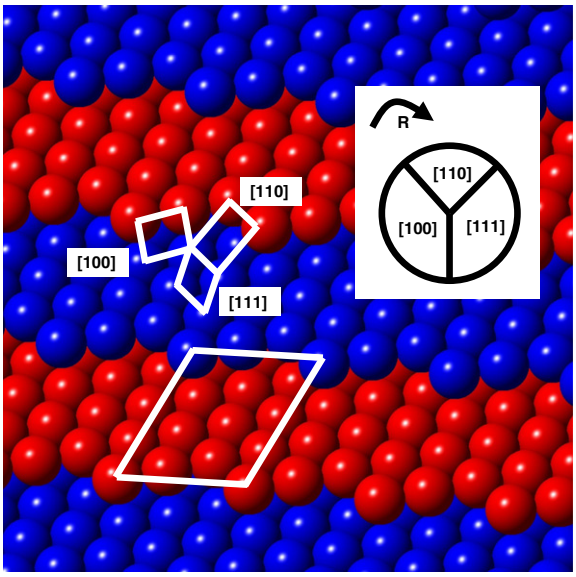

Fig. 1. Cartoon of the ideal $(643)^R$ surface, with downward steps from the top to the bottom of the image. Alternate layers are coloured red and blue to aid visualisation of the surface. The figure shows the unit cells of the micro facets: the step site is [100], the kink site is [110] and the terrace is [111]. The handedness of the surface is defined as indicated by the schematic in the top right, which here indicates a clockwise orientation of priority, from [100] steps to [110] kinks then [111] terraces, and is assigned as the R-enantiomer [18]. The parallelogram at the bottom of the image indicates the (643) unit cell. (For interpretation of the references to colour in this figure legend, the reader is referred to the web version of this article.)

(i.e. stepped) surfaces. Most notably, deposition of metallic Ag on Cu(223) induces a periodic faceting of the underlying Cu surface into a "hill and valley" structure [28–32], whilst adsorption of oxygen and sulfur are both known to drive substantial mass-transfer and faceting of Cu surfaces [33–38]. These systems can be expected to have similarities with the deposition of Te, a metalloid chalcogen, as will be described here. However, a significant difference between the present study and previous thin film growth on chiral substrates is that we observe alloying and the formation of the compound copper telluride as a nanoscale film. The present study therefore provides a unique method for the production of chirally-structured transition metal chalcogenide films, which are potentially useful models for the study of chirality in the electronic properties of topological insulators.

2. Experimental

Measurements were performed in two separate UHV systems, both with an operating pressure of 2×10^{-10} mbar. The first chamber was equipped with a discharge lamp (VG Scienta Ltd.) which provides He(I) radiation for ultraviolet photoemission spectroscopy (UPS) and an Al K_α X-ray source (VG Scienta Ltd.) for x-ray photoemission spectroscopy (XPS). Spectra were collected using a concentric hemispherical analyser (CLAM 2, VG Scienta Ltd.) aligned along the macroscopic normal of the $Cu(643)^R$ surface. The second chamber was used to collect STM data. STM images were obtained using an Omicron STM-1 with MATRIX software, using an etched W tip with a positive bias in constant height mode. The $Cu(643)^R$ sample was cleaned *in-situ* by repeated cycles of Ar^+ bombardment (1 kV, 8 μA) and annealing to 830 K. Sample cleanliness and crystallinity were verified by XPS and LEED. Te was deposited from a homemade Knudsen effusion cell. For sub monolayer (ML) films, the typical cell temperature was 570 K. The deposition rate for sub monolayer films was calculated from Cu $2p^{3/2}$ and Te $3d^{5/2}$ XPS intensities to be ~0.2 ML min^{-1}. For film thicknesses greater than 10 ML, a cell temperature around 610 K was used, giving a deposition rate of ~5 ML min^{-1}. Te coverages quoted here have an approximate error of ±0.05 ML and are given with respect to the atomic density of the Cu(111) surface.

3. Results

The LEED pattern obtained from an atomically clean Cu(643) surface is shown in the first panel of Fig. 2 and is assigned as $Cu(643)^R$ by comparing it to a $Pt(643)^R$ pattern reported previously [8]. The pattern can be considered as an off-axis 6-fold pattern of split spots, with the off-axis 6-fold pattern arising from the (111) terraces of Fig. 1 and the spot splitting arising from the longer-range periodicity of the stepped surface [8,19,39]. This spot splitting breaks the symmetry of the LEED pattern and the angle of the doublet with respect to the 6-fold pattern can be used to assign surface chirality [8]. Images of LEED patterns collected after room temperature deposition of up to 1.5 ML are displayed in subsequent panels of Fig. 2. All of these patterns were collected after the surface was annealed at 773 K for 10 min, then allowed to cool slowly back to 110 K, a procedure adopted because patterns collected immediately after deposition at 300 K were diffuse, implying a significant amount of disorder and/or surface mobility. Notably, the annealing process does not change the chemical identity of the surface for low coverages, since there was no induced change in peak shape or intensity in the XPS spectra. Thus, it is likely that local ordering occurs immediately upon deposition, but at a length scale too small to be observed with LEED, and perhaps with a number of isolated defects that attenuate coherent electron scattering in LEED. Surface homogeneity then improves with annealing, suggesting that the substantial mass transfer associated with the faceting reconstructions described below is kinetically limited at room temperature. An overview of Cu $2p^{3/2}$ and Te $3d^{5/2}$ XPS spectra, corresponding roughly to the coverages of Fig. 2 and collected at a sample temperature of 300 K, is shown in Fig. 3. Each Te $3d^{5/2}$ and Cu $2p^{3/2}$ spectrum was fitted to the sum of Gaussian and Doniach Sunjic (DS) functions [40] and the fitted binding energies were in agreement

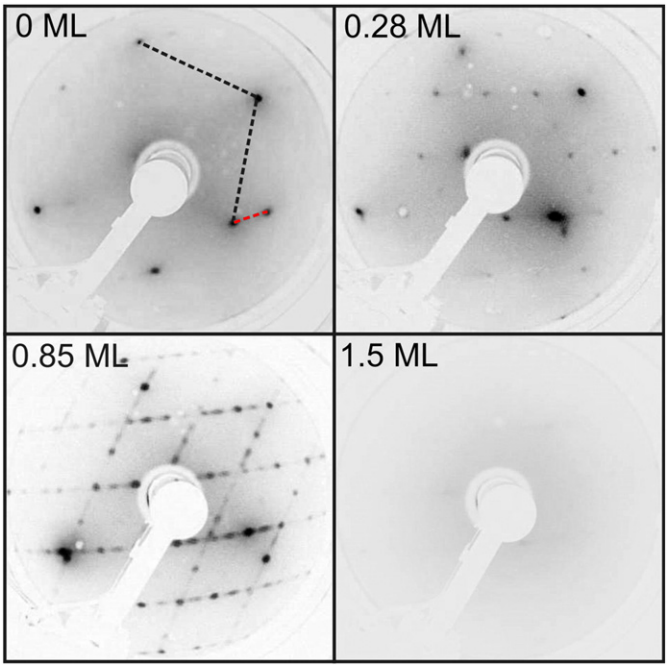

Fig. 2. LEED patterns obtained for increasingly thicker Te films on $Cu(643)^R$, recorded at a sample temperature of 110 K. The top left panel shows the clean $Cu(643)^R$ surface with the dashed black line indicating part of the $(643)^R$ surface unit cell. The dashed red line shows that the (0,1) spot has been split by a length inversely proportional to the step separation. All spots in the clean $Cu(643)^R$ pattern are split, however, they are difficult to see at a single beam energy. The beam energy in all images is 138 eV. (For interpretation of the references to colour in this figure legend, the reader is referred to the web version of this article.)

Please cite this article as: M.O. King, et al., The templated growth of a chiral transition metal chalcogenide, Surf. Sci. (2014), http://dx.doi.org/10.1016/j.susc.2014.02.008

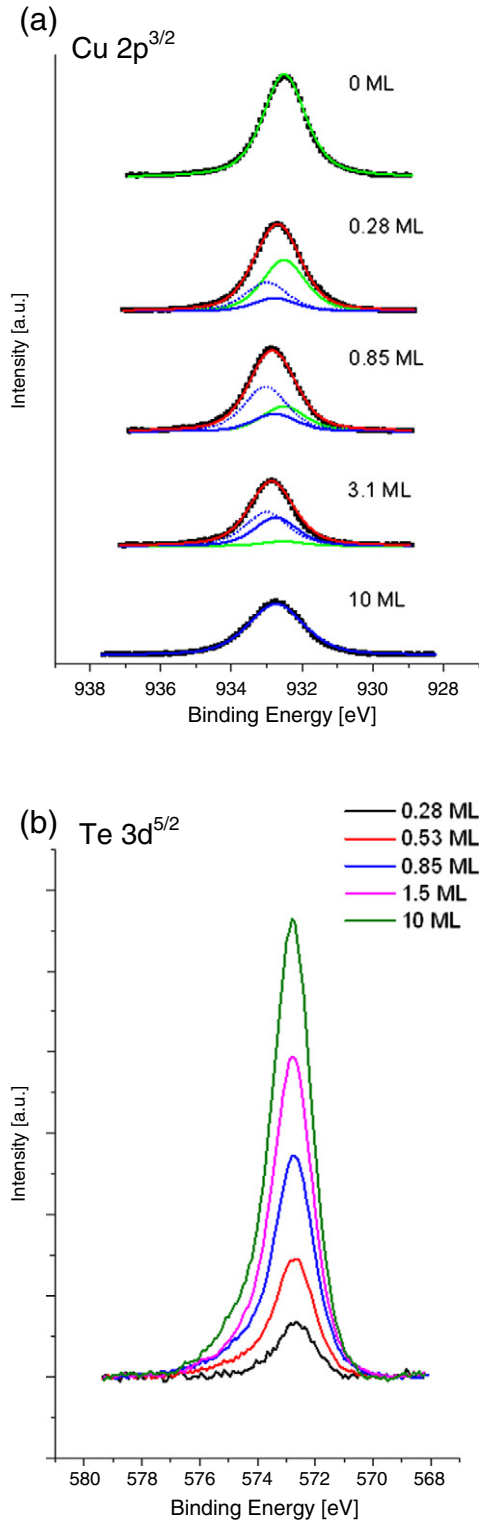

Fig. 3. a) XPS spectra for the Cu $2p^{3/2}$ core level. Each panel is a spectrum obtained after deposition at room temperature, followed by an anneal at 773 K then a slow cool back to 300 K. The green line is elemental Cu, the solid blue line is ionic Cu^{+} and dashed blue line is Cu^{2+}. b) XPS spectra for the Te $3d^{5/2}$ core level. Spectra were collected under identical conditions to those from Cu $2p^{3/2}$. The binding energy of this peak is 572.7 eV, corresponding to Te^{2-}. (For interpretation of the references to colour in this figure legend, the reader is referred to the web version of this article.)

with previous studies of copper and tellurium systems [41–44]. The width and asymmetry of each peak were fixed to those obtained from an elemental Cu or Te film, the values of which can be found in Table 1 (supplementary information). Thus, for example, Cu $2p^{3/2}$ XPS spectra were fitted to a series of functions representing elemental $Cu^{(0)}$, Cu^{+} and Cu^{2+}. The widths and asymmetries of Cu^{+} and Cu^{2+} were fixed to those of $Cu^{(0)}$ and their binding energies were fixed to those of similar Te and Cu compounds. The goodness of fits to various known alloy phases are also given in the supplementary information. The stoichiometry of the film was calculated using the method outlined in reference [45] and using the intensities of the XPS signals from the Cu $2p^{3/2}$ and Te $3d^{5/2}$ core levels. We used a stoichiometric polycrystalline Cu_2Te film as a reference to calibrate the relative sensitivity factors for the electron analyser. UPS data were also collected from each film discussed below and are presented in the supplementary information. The combination of the above measurements, in addition to STM images, provides a comprehensive understanding of the initial stages of Te deposition. Since we find these data sets to naturally fall into three main structural regimes, they will be discussed regime-by-regime below.

3.1. Structure 1 ($0.18 < \theta_{Te} < 0.45$ ML)

The first ordered LEED pattern was observed for Te coverages in the range of 0.18 ML to 0.45 ML and was sharpest at 0.28 ML (Fig. 2). A progressive degradation in pattern quality was observed above 0.28 ML, until extra spots started to emerge at 0.45 ML (see below). On first appearances, the LEED patterns seem rhombohedral, however bright spots do not necessarily appear at the rhombohedral apexes. Instead, a qualitative analysis of the diffraction patterns as a function of beam energy reveals them to be better described as the incoherent summation of two distinct patterns, one accounting for spots lying on horizontal lines and the other accounting for spots on diagonal lines. As the incident beam energy was increased, the spots lying on horizontal lines moved left to right whilst those spots on diagonal lines moved from bottom left to top right, giving the appearance of spots passing through each other at specific energies (see supplementary information). This behaviour differs from that expected from a flat, low Miller index surface, where increasing the energy of an electron beam at normal incidence will move diffraction spots radially inwards, as viewed on a rear-view LEED system such as that used here. Instead, the lateral motion of diffraction spots is consistent with an off-axis scattering geometry or, as we believe to be the case here, diffraction from a micro-facetted surface, with two sets of well-defined facets, each inclined to the surface normal (and hence the incident beam), giving rise to two sets of diffraction spots. This interpretation is consistent with STM images, as discussed below, and is common to a number of previous spot profile analysis LEED studies of other vicinal systems [46–50]. A schematic interpretation of the LEED pattern at 0.28 ML, colouring horizontal spots in red and diagonal spots in blue, and indicating their respective reciprocal lattice vectors, is presented in Fig. 4a. The resulting unit cells form mirror-image oblique lattices with corresponding real-space parameters of $a_1 = 0.51 \pm 0.01$ nm, $b_1 = 0.71 \pm 0.01$ nm and an acute internal angle, $\alpha_1 = 60°$. The presence of oblique lattices indicates surface chirality in the two domains and the dominance of the horizontal spots–which are bright–over the generally weak diagonal spots suggests that one enantiomer (*i.e.* one facet orientation) dominates the surface structure. An asymmetry in the proportion of facets is to be expected if the macroscopic miscut angle is to be maintained. Indeed, one simple faceting transition of $Cu(643)^R$ would be the formation of close-packed facets bounded by ridges that are produced by a regular alignment of the original kink sites. Preserving the macroscopic miscut angle implies that the facets would be mirror-symmetric in all but size. It is beyond the scope of the present work to perform a full IV analysis of the diffracted intensities and thereby assign the atomic positions in the surface layer; indeed, the substantial mass-transfer required for micro-faceting is known to complicate LEED IV analysis [51] and diffracted intensities from microfacets will also vary strongly with angular positioning of the sample. However, a combination of

Please cite this article as: M.O. King, et al., The templated growth of a chiral transition metal chalcogenide, Surf. Sci. (2014), http://dx.doi.org/10.1016/j.susc.2014.02.008

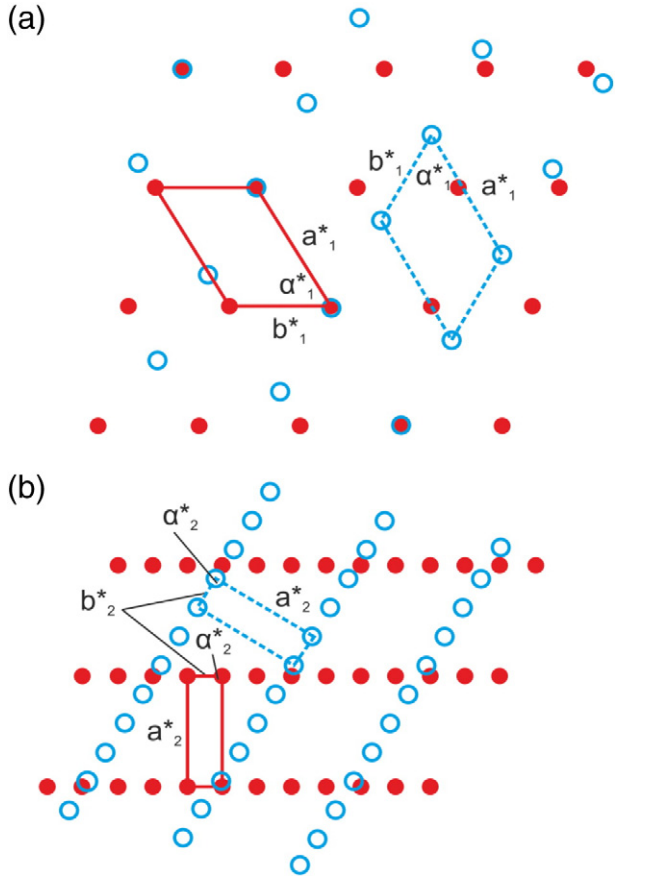

Fig. 4. Schematic representations of the LEED patterns obtained from the deposition of Te on Cu(643)^R. The solid red circles and the hollow blue circles represent LEED patterns from two different domains present on the surface. (a) is a schematic of the 0.28 ML coverage, whilst (b) is a schematic of the 0.85 ML coverage. Annotations indicate the reciprocal cell dimensions measured for both domains.

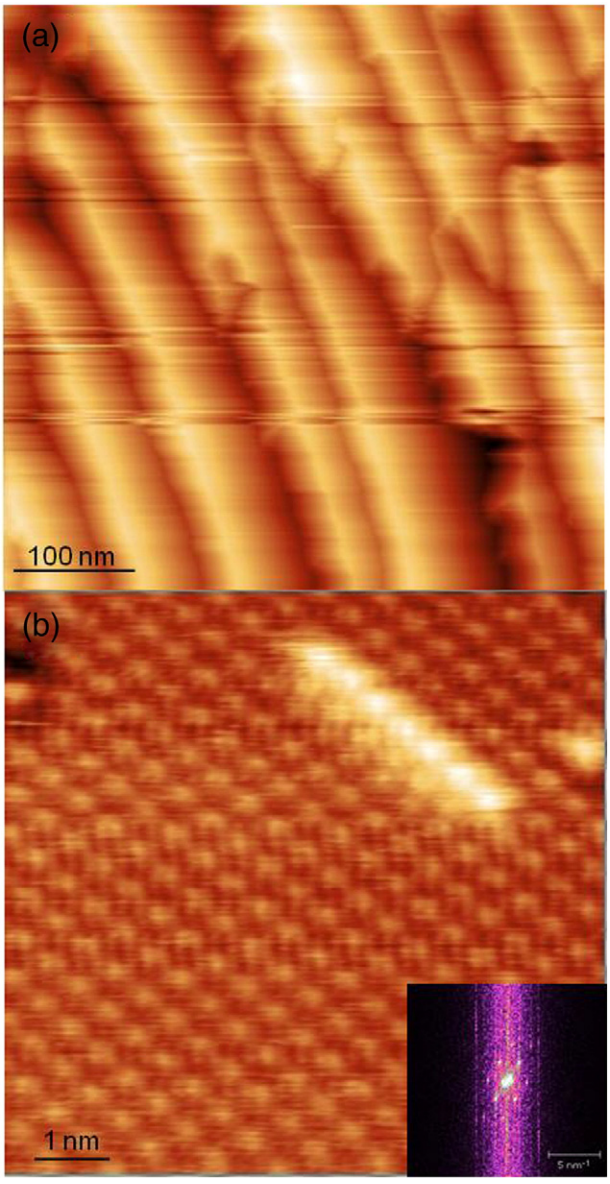

Fig. 5. STM of 0.28 ML Te/Cu(643)^R deposited at 300 K, annealed to 773 K for 10 min and then allowed to cool to 300 K for STM acquisition. The tip parameters were $I_t = 900$ pA and $V_{gap} = 1.1$ V in both images. (a) shows a low magnification image of the facetted surface. (b) is a higher magnification image showing atomic corrugations with (inset) its fast Fourier transform.

STM and XPS provide strong evidence of a particular alloy phase, as outlined below.

Te XPS data collected from the 0.28 ML Te/Cu(643)^R film were well fitted with a single Gaussian-DS function, with a binding energy matching that of bulk Te^{2-}(572.7 eV), and therefore suggests that the Te atoms are incorporated into a bulk-like alloy immediately upon deposition rather than occupying adsorption sites or forming a surface substitutional alloy. This is in contrast to the growth of Te on low miller index Cu surfaces (Cu(111) [52,53] and Cu(100) [53]), where Te initially resides on the surface and has a distinct chemical shift (to 572.3 eV) in XPS. Immediate alloying is not particularly surprising as vicinal surfaces are known to lower alloy transition temperatures, with adatom diffusion into the bulk via the low energy pathway provided by under co-ordinated step atoms [53–57].

The fit to the 0.28 ML Cu $2p^{3/2}$ XPS data yields a Cu^+:Cu^{2+} ratio of 1:2.2 ± 0.1, which does not match any common alloy (see supplementary information) and so suggests a mixture of phases. The most likely mix is a 2.2:1 ratio of CuTe and Cu_2Te, the latter of which will be shown to exist at higher coverages ($\theta_{Te} > 1$ ML). The measured stoichiometry gives a Cu:Te ratio of 1.3 ± 0.1:1, which is also consistent with a mixture of CuTe and Cu_2Te.

Turning to the STM data, the low magnification image of Fig. 5a reveals substantial faceting of the Cu(643)^R surface after deposition of 0.28 ML Te, in agreement with the interpretation of LEED data presented above. The surface is clearly heterogeneous, with poorly-ordered facets up to 150 nm wide, typical peak-to-valley variations of 5 nm and a geometry that suggests (111)-like orientations. The production of two facet orientations but predominance of one facet orientation over another is consistent with the two distinct sets of spots observed in LEED with different intensities and also with the geometric requirement that the surface's macroscopic miscut angle is preserved. The angle of the facets from the (643) plane was ~16°, which is approximately the angle to a (111)-like plane. The presence of sharp LEED spots and the XPS data indicate the facets to be terminated by well-ordered, flat alloys, in agreement with the high resolution image of Fig. 5b. This atomic resolution STM image was obtained from a 0.28 ML surface at 300 K, which is interesting as it again suggests a change in the chemical identity of the surface because previous studies of the clean Cu(643)^R surface only achieve atomic resolution at cryogenic temperatures, once adatom motion is quenched [27]. As with our previous study of Te/Cu(111) [52], care has to be taken when assigning chemical identity to the protrusions in bimetallic thin films. In previous electrochemical STM studies of Te, (e.g. Te/Pt(111) [58,59]), Te adatoms were imaged as bright protrusions with a positively biased tip and this gives confidence to

Please cite this article as: M.O. King, et al., The templated growth of a chiral transition metal chalcogenide, Surf. Sci. (2014), http://dx.doi.org/10.1016/j.susc.2014.02.008

the assignment of the bright protrusions as Te atoms here. In contrast to our earlier study of Te/Cu(111), however, neither the STM images nor the XPS data indicate the presence of a $(2\sqrt{3} \times \sqrt{3})$ or $(\sqrt{3} \times \sqrt{3})$ surface substitutional alloy. Instead, the initial presence of steps, coupled with the substantial mass transfer implied by faceting, has facilitated full alloy formation. The apparent Te coverage of the 0.28 ML Te/Cu(643)^R surface can be estimated from the density of bright spots in Fig. 5b. Defining 1 ML with respect to a layer of Cu(111) surface, the surface coverage is calculated to be 0.18 ± 0.05 ML, which is ~35% lower than that measured by XPS and therefore indicative of the alloy extending beyond the first atomic layer. Also present in the STM image of Fig. 5b is a row of protrusions (the brightest features) which may be the start of the next layer of alloy. Unfortunately, sample drift is evident, limiting accuracy of structural measurements. The bright protrusions in Fig. 5a give a measured unit cell of $a_1 = 0.6 \pm 0.1$ nm and $b_1 = 0.7 \pm 0.1$ nm, with the acute internal angle measured as $\alpha_1 = 57 \pm 4°$, in reasonable agreement with the unit cell parameters measured with LEED. As the LEED images indicate a small proportion of the opposite enantiomer to be present, we infer it to exist on facets oriented in the other direction to that imaged.

3.2. Structure 2 ($0.45 < \theta_{Te} < 1.5$ ML)

A second ordered structure, labelled Structure 2, becomes visible with LEED above 0.45 ML and is most sharp at 0.85 ML, as illustrated in Fig. 2. The pattern again comprises two distinct sets of spots that move through one another with increasing electron energy. The intensities of the two patterns are more similar than at lower coverages, which is surprising if they relate to a similar asymmetric faceting that is again constrained by the underlying crystal's miscut angle. A more quantitative analysis would be required to address this observation in more detail. A number of additional spots have appeared between those observed at 0.28 ML (but still lie on the same lines) and there is some streaking evident, which is consistent with superstructure formation along one axis, but with variable periodicity. Fig. 4b separates schematically the two sets of spots, using the same red–blue colour scheme as above, and further LEED images are presented in the supplementary information. The close separation of spots, their streaked nature and the variations in intensity due to the surface corrugation and scattering geometry preclude a definitive assignment of reciprocal unit cell geometry from the LEED patterns alone. The mutual angle between reciprocal lattice vectors is determined to be $\alpha_2 = 85 \pm 7°$, which is too wide an error margin to determine unambiguously if the structure is chiral; however, interpretation of the STM images (discussed below) is clearer.

The Te $3d^{5/2}$ XPS spectrum from the 0.85 ML Te/Cu(643)^R surface is shown in Fig. 3a. It could also be fitted by a single function with a binding energy of 572.7 eV, corresponding to bulk Te^{2-} and indicating similar Cu–Te bonding to that at 0.28 ML. The fit to the Cu $2p^{3/2}$ spectrum (Fig. 3b) yields a ratio of Cu^+:Cu^{2+} of 1:3.1 ± 0.1, indicating that the surface is rich in Cu^{2+} but again does not correspond to a known Cu–Te alloy, implying surface inhomogeneity and the presence of a mixture of CuTe and Cu_2Te, with an estimated ratio of 3.1:1, i.e. more CuTe than at 0.28 ML. Notably, there is no evidence for the formation of Cu_3Te_2, an alloy identified as forming when Te is deposited onto flat Cu(111) [52].

Fig. 6a shows an STM image taken from a surface prepared from 0.85 ML of Te/Cu(643)^R that has been annealed to 773 K for 10 min, then slowly cooled to 300 K. It reveals that the surface again appears facetted, but has greater regularity than at lower coverages. The facets in the image are typically ~30 nm wide, have a peak-to-valley distance of around 2 nm and have an orientation that suggests that the steps accommodate a small ~5° misalignment with respect to (111) planes. Interestingly, and different to the lower-coverage surface, the facets are not atomically smooth, but are themselves punctuated by multiple small steps that are 2–3 nm wide and 0.09 nm tall, as illustrated in Fig. 6b. The structure bears some similarity to the multiply-stepped structures observed on nitrided Cu(100) [60] and the contrast differs from that observed at lower coverages, indicating a change in chemical character. There is variability in the terrace width, which typically spans either four or five repeating units. Considering the whole terrace as a 'unit cell', the dimensions are measured to be $a_1 = 0.54 \pm 0.05$ nm, $b_2 = 2.20 \pm 0.05$ nm (4 cell wide terrace) or $b_2 = 2.71 \pm 0.05$ nm (5 cell wide terrace) and $\alpha_2 = 88 \pm 3°$ in both cases. The 4 atom wide terrace is in excellent agreement with the dimensions extracted from the LEED pattern of Fig. 2, which are $\alpha_2 = 0.46 \pm 0.01$ nm, $b_2 = 2.21 \pm 0.10$ nm and $\alpha_2 = 87 \pm 3°$. The angle α_2 is within error of 90° and thus we interpret the unit cell as being rectangular and therefore achiral, with the variations in step width accounting for the streaking in the b_2 direction observed with LEED.

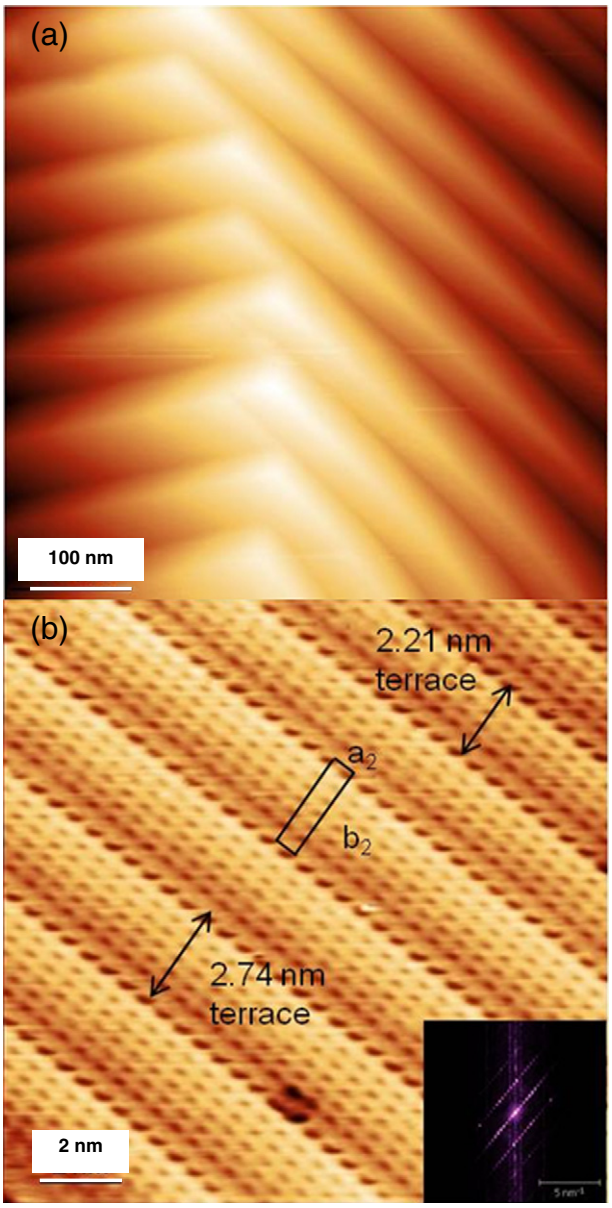

Fig. 6. STM images of 0.85 ML Te/Cu(643)^R, deposited at 300 K, annealed to 773 K for 10 min and then allowed to cool to 300 K for STM acquisition. The tip parameters were $I_t = 800$ pA and $V_{gap} = 1.1$ V in both images. (a) Large-scale faceting is evident in the low magnification image, whilst higher magnification images of a single terrace (b) indicate atomic-scale ordering and steps. Annotations indicate the measured surface unit cell dimensions.

3.3. Disordered Phase ($\theta_{Te} > 1.5$ ML)

LEED patterns obtained above a 1.5 ML Te coverage showed no sharp spots (Fig. 2) and became progressively weaker. Te $3d^{5/2}$ XPS data collected for Te coverages greater than 0.85 ML (Fig. 3) were again fitted to a single function at 572.7 eV, representing a bulk alloy of Te^{2-} without other alloy components. For 10 ML Te coverage, the Cu $2p^{3/2}$ spectra were well fitted by a single function, corresponding to Cu^{+}, the only Cu oxidation state present in Cu_2Te. The XPS data yield a ratio of ionic Cu to Te of 2.1 ± 0.1, which is within error of stoichiometric Cu_2Te. The XPS data show a gradual transition from a predominantly CuTe surface to a Cu_2Te surface with increasing Te coverage. UPS spectra (see supplementary data) collected from thick Te films indicates alloying [52], however they lack the fine structure to make an assignment of Cu–Te stoichiometry. On first inspection, it may seem surprising that increasing the Te coverage results in a surface phase that is richer in Cu. However, thermodynamic analysis [61] of the Cu–Te alloy system indicates that the formation of Cu_2Te is more favourable than of CuTe and our previous work [52] has shown Cu to be mobile within CuTe alloys. Since the intermixing of Cu and Te is facile at 300 K, there are no kinetic barriers to achieving the thermodynamically-favoured alloy. Thus, as the Te film gets thicker, the surface has less influence on the nature of the Cu–Te alloy and allows for the thermodynamically more stable alloy to form, Cu_2Te. Indeed, Cu_2Te is commonly observed for the deposition of thick Te films on polycrystalline Cu [62,63].

3.4. Temperature Dependence of Alloying

The temperature dependence of alloying was monitored by depositing a thick 30 ML Te film at 110 K, a temperature that was too low to permit alloying and a coverage that was sufficient to completely attenuate the Cu $2p^{3/2}$ XPS signal. The substrate was then annealed for 10 min at sequentially higher temperatures and Cu $2p^{3/2}$ and Te $3d^{5/2}$ XPS data were collected whilst cooling, with results summarised in Fig. 7. Both the Te $3d^{5/2}$ binding energy and the Cu $2p^{3/2}$ intensity indicate a single sharp alloying transition at 225 K. Above this annealing temperature the binding energy of Te $3d^{5/2}$ shifts from 573.1 eV, which is characteristic of elemental Te, to 572.7 eV, which is characteristic of the bulk alloy of Cu_2Te [43]. Thermodynamically, alloying of Cu and Te is favourable even at 110 K but, as we have previously observed in Te/Cu(111), it is kinetically inhibited below the transition temperature, which here is around 50 K lower than that observed on flat Cu(111) [52]. This reduction is consistent with the step sites providing a lower kinetic energy barrier to alloying and diffusion into the bulk than directly into a (111) surface, as observed in a number of other vicinal systems.

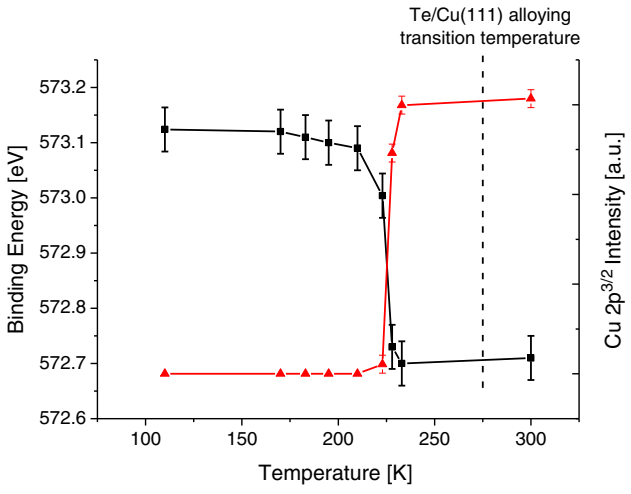

Fig. 7. The variation of Te $3d^{5/2}$ binding energy (black line) and Cu $2p^{3/2}$ XPS intensity (red line) with temperature for a Te coverage of 30 ML that was initially deposited at 110 K. A single sharp transition was observed at 225 K. The dashed black line is the alloying transition temperature measured previously [52] for 30 ML Te/Cu(111), which is 275 K. (For interpretation of the references to colour in this figure legend, the reader is referred to the web version of this article.)

4. Discussion

The XPS, LEED and STM data provide a coherent picture of the alloying of Te on $Cu(643)^R$. A summary of the alloy phases, as derived from the above discussion of XPS analysis, is presented in Fig. 8. The data show a continuous attenuation of the copper XPS signal with increasing Te coverage, until equilibrium is achieved. The results are consistent with formation of CuTe, which implies substantial migration of buried Cu towards the surface (or, conversely, migration of newly-deposited Te into the bulk). A bulk-like CuTe alloy forms in the very early stages of deposition, in contrast to the formation of a surface alloy on Cu(111), but presumably mediated by the low-energy pathways for direct incorporation of Te into terraces provided by the surface steps. There is a clear switch towards Cu_2Te formation by a coverage of 0.45 ML, after which the proportion of Cu_2Te increases largely linearly with Te coverage. Interestingly, the formation of Cu_2Te was also observed for the deposition of Te on polycrystalline Cu [62]. The alloying process clearly induces faceting of the high index single crystal surface; both the level of the restructuring of the surface and the nature of the alloy formed is strongly dependent on the amount of Te deposited. STM images collected from Structures 1 and 2 clearly demonstrate a dramatic change in the structure of the facets, from flat terraces in Structure 1 to stepped terraces in Structure 2. Such a gross change in the structure necessitates significant mass transport across the surface, which is common to many vicinal systems upon deposition of an overlayer, including O, N and S [33–38,60].

Structure 1 has an oblique lattice which is inherently chiral; both enantiomers are observed in LEED, albeit with one displaying more

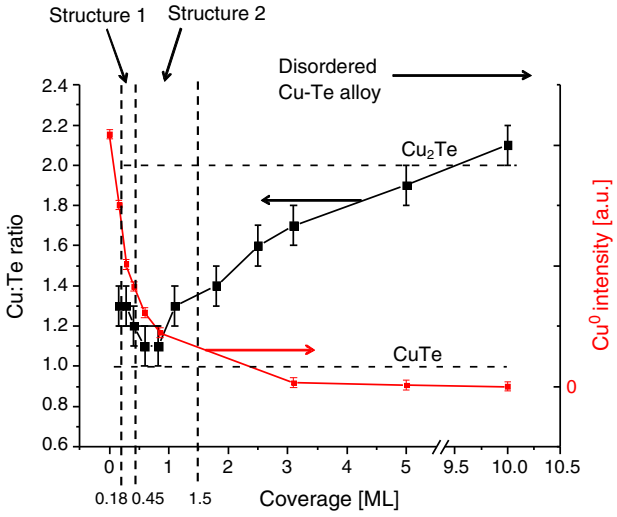

Fig. 8. Summarised growth of Te/$Cu(643)^R$ after depositing at 300 K and annealing to 773 K, using XPS data to illustrate trends and indicating (top) the main structural phases that have been identified. The black line shows the change in the stoichiometry of the Cu–Te film as a function of Te coverage (left-hand ordinate, black arrow). The red line shows the change in intensity of the elemental Cu peak as a function of Te coverage (right-hand ordinate, red arrow). Elemental Cu intensity decays monotonically as the growing alloy thickens and attenuates the substrate photoemission. The horizontal dashed black lines indicate the Cu:Te ratio for CuTe and Cu_2Te and do not apply to the Cu^0 intensity plot. (For interpretation of the references to colour in this figure legend, the reader is referred to the web version of this article.)

Please cite this article as: M.O. King, et al., The templated growth of a chiral transition metal chalcogenide, Surf. Sci. (2014), http://dx.doi.org/10.1016/j.susc.2014.02.008

intense diffraction spots. Chen et al. [64] commented in their study on the adsorption of R- and S-phenylglycine on Cu(110) that the ratio of R/S mixture is directly related to the relative intensity of the LEED spots, for the R- and S-patterns. For example, a coverage of R- and S-phenylglycine with the ratio of R/S = 1 gave LEED spot intensities that were similar and for a ratio of R/S = 3, the LEED spots from the R enantiomer were much more intense. In our study, Structure 1 gives an intensity ratio of ~4:1 between the different surface alloy enantiomers. The observation of an enantiomeric excess in Structure 1 can only come about if some level of the chirality of the $Cu(643)^R$ surface is retained after faceting, thereby providing the chiral influence required to make one of the enantiomeric structures slightly more energetically favourable. With the data available, we can only speculate on the nature of the chiral influence at play with Structure 1. We speculate that the mesoscopic facets are bound by chiral kinks and steps because the macroscopic miscut of the surface must be maintained. These kinks would be expected to provide a weak chiral influence on the overlayer and thus the handedness of the surface. This proposal would appear to fit with the fact that the alloying of Te on $Cu(643)^R$ is strongly influenced by the kink and step sites of the native surface, as evidenced by the different behaviour observed on Cu(111) [52]. In the same way as for Structure 1, the intensity of equivalent spots can be measured on the LEED patterns of Structure 2 to estimate the relative populations of the two domains: it was found that within experimental error both domains are populated equally. Clearly, with increasing Te deposition and increasing alloy film thickness, the chiral influence diminishes or disappears altogether and the alloy adopts a double domain structure with an achiral rectangular unit cell. In essence, the alloy overlayer decouples from the structure of the underlying chiral substrate and with increasing alloy thickness could in some senses be regarded as a 'floating overlayer' with a structurally complex (and likely diffuse) buried interface between alloy and substrate.

Structures 1 and 2 have stoichiometries that do not coincide with a single phase of copper telluride alloy with an available bulk crystal structure, nor do they have lattice vectors that are related to the $Cu(643)^R$ substrate lattice vectors through simple geometric relations. Consequently, we cannot simply interpret the surface structures observed here as the termination of a known copper telluride phase without exploring further the level of structural/compositional heterogeneity within the alloy film. However, although we lack evidence to propose unambiguous structures for the two ordered phases, we can speculate on the origin of the chirality displayed by Structure 1. All known bulk copper tellurides alloys have unit cells with achiral space groups and so these materials can only display chiral surfaces if an intrinsically chiral high Miller index surface plane is exposed. If this was the case for Structure 1, it would have kink sites that convey chirality on to the film. However the observed STM images of Structure 1 provide no evidence for chiral kink sites. Therefore, we propose that the chirality of Structure 1 arises because the alloy itself has an intrinsically chiral structure. Consequently, we suggest that the $Cu(643)^R$ surface initially templates the growth of a metastable chiral copper telluride alloy that has no known bulk counterpart.

5. Conclusions

We have demonstrated that nanoscale chiral copper telluride alloy films with an excess of one enantiomer can be grown on a chiral cut of a single crystal surface. The residual influence of the chiral kink on the growth diminishes with the thickness of the alloy; eventually an achiral structure, with a rectangular unit cell is formed. Our work provides a route for the preparation of chiral nanoscale (transition metal chalcogenide) films that could have potential uses in the study of topological insulators.

Acknowledgements

We thank the University of Glasgow for the provision of both a studentship (MOK) and travel funds to attend the Australian Synchrotron. The Engineering and Physical Sciences Research Council is thanked for the provision of studentships (IMM and DH) and a fellowship (DAM, EP/I00419X/1).

Appendix A. Supplementary data

Supplementary data to this article can be found online at http://dx.doi.org/10.1016/j.susc.2014.02.008.

References

[1] C.J. Baddeley, Top. Catal. 25 (2003) 17.
[2] R. Popa, J. Mol. Evol. 44 (1997) 121.
[3] D. Hsieh, Y. Xia, L. Wray, D. Qian, A. Pal, J.H. Dil, J. Osterwalder, F. Meier, G. Bihlmayer, C.L. Kane, Y.S. Hor, R.J. Cava, M.Z. Hasan, Science 323 (2009) 919.
[4] X.Y. Zhao, J. Am. Chem. Soc. 122 (2000) 12584.
[5] J.A. Switzer, H.M. Kothari, P. Poizot, S. Nakanishi, E.W. Bohannan, Nature 425 (2003) 490.
[6] R. Raval, Chem. Soc. Rev. 38 (2009) 707.
[7] M.O. Lorenzo, S. Haq, T. Bertrams, P. Murray, R. Raval, C.J. Baddeley, J. Phys. Chem. B 103 (1999) 10661.
[8] S.J. Jenkins, S.J. Pratt, Surf. Sci. Rep. 62 (2007) 373.
[9] C.F. McFadden, P.S. Cremer, A.J. Gellman, Langmuir 12 (1996) 2483.
[10] Y.J. Yun, A.J. Gellman, Angew. Chem. Int. Edit. 52 (2013) 3394.
[11] Y. Huang, A.J. Gellman, Catal. Lett. 125 (2008) 177.
[12] J.D. Horvath, L. Baker, A.J. Gellman, J. Phys. Chem. C 112 (2008) 7637.
[13] D.M. Rampulla, A.J. Gellman, Surf. Sci. 600 (2006) 2823.
[14] H.S. Lee, J.S. Park, B.M. Kim, S.H. Gellman, J. Org. Chem. 68 (2003) 1575.
[15] J.D. Horvath, A.J. Gellman, J. Am. Chem. Soc. 123 (2001) 7953.
[16] O.A. Hazzazi, C.A. Harris, P.B. Wells, G.A. Attard, Top. Catal. 54 (2011) 1392.
[17] O.A. Hazzazi, G.A. Attard, P.B. Wells, J. Mol. Catal. A Chem. 216 (2004) 247.
[18] G.A. Attard, J. Phys. Chem. B 105 (2001) 3158.
[19] A. Ahmadi, G. Attard, J. Feliu, A. Rodes, Langmuir 15 (1999) 2420.
[20] C. Fleming, M. King, M. Kadodwala, J. Phys. Chem. C 112 (2008) 18299.
[21] A.J. Francis, A.J. Koritnik, A. Gellman, P.A. Salvador, Surf. Sci. 601 (2007) 1930.
[22] A.J. Francis, P.A. Salvador, Ceram. Trans. 158 (2005) 37.
[23] A.J. Francis, P.A. Salvador, J. Appl. Phys. 96 (2004) 2482.
[24] R.S. Cahn, C. Ingold, V. Prelog, Angew. Chem. Int. Edit. 5 (1966) 385.
[25] D.S. Sholl, A. Asthagiri, T.D. Power, J. Phys. Chem. B 105 (2001) 4771.
[26] T.D. Power, A. Asthagiri, D.S. Sholl, Langmuir 18 (2002) 3737.
[27] A.E. Baber, A.J. Gellman, D.S. Sholl, E.C.H. Sykes, J. Phys. Chem. C 112 (2008) 11086.
[28] A.R. Bachmann, F. Ostendorf, S. Speller, J. Phys. Condens. Matter 15 (2003) S3337.
[29] J. Lobo, E.G. Michel, A.R. Bachmann, S. Speller, L. Roca, J. Kuntze, J.E. Ortega, J. Vac. Sci. Technol. A 21 (2003) 1194.
[30] A.R. Bachmann, S. Speller, A. Mugarza, J.E. Ortega, Surf. Sci. 526 (2003) L143.
[31] J.E. Ortega, A. Mugarza, A. Narmann, A. Rubio, S. Speller, A.R. Bachmann, J. Lobo, E.G. Michel, F.J. Himpsel, Surf. Sci. 482 (2001) 764.
[32] A. Coati, J. Creuze, Y. Garreau, Phys. Rev. B 72 (2005) 115424.
[33] T. Brandstetter, M. Draxler, M. Hohage, P. Zeppenfeld, Phys. Rev. B 76 (2007) 245420.
[34] E. Vlieg, S.M. Driver, P. Goedtkindt, P.J. Knight, W. Liu, J. Ludecke, K.A.R. Mitchell, V. Murashov, I.K. Robinson, S.A. de Vries, D.P. Woodruff, Surf. Sci. 516 (2002) 16.
[35] N. Reinecke, S. Reiter, S. Vetter, E. Taglauer, Appl. Phys. A Mater. Sci. Process. 75 (2002) 1.
[36] P.J. Feibelman, Phys. Rev. Lett. 85 (2000) 606.
[37] W.L. Ling, N.C. Bartelt, K. Pohl, J. de la Figuera, R.Q. Hwang, K.F. McCarty, Phys. Rev. Lett. 93 (2004) 166101.
[38] G.B.D. Rousseau, A. Mulligan, N. Bovet, M. Adams, V. Dhanak, M. Kadodwala, Surf. Sci. 600 (2006) 897.
[39] X. Zhao, S.S. Perry, J. Mol. Catal. A Chem. 216 (2004) 257.
[40] S. Doniach, M. Sunjic, J. Phys. C 3 (1970) 285.
[41] H. Neumann, M. Mast, J. Enderlein, R.D. Tomlinson, M.V. Yakushev, Cryst. Res. Technol. 31 (1996) 75.
[42] A.J. Ricco, H.S. White, M.S. Wrighton, J. Vac. Sci. Technol. A 2 (1984) 910.
[43] Y. Zhang, Z.P. Qiao, X.M. Chen, J. Mater. Chem. 12 (2002) 2747.
[44] S. Hufner, G.K. Wertheim, J.H. Wernick, Solid State Commun. 17 (1975) 417.
[45] C.J. Powell, A. Jablonski, J. Electron Spectrosc. Relat. Phenom. 178 (2010) 331.
[46] H. Minoda, T. Shimakura, K. Yagi, F.-J. Meyer zu Heringdorf, M. Horn von Hoegen, Phys. Rev. B 61 (2000) 5672.
[47] M. Czubanowski, A. Schuster, S. Akbari, H. Pfnür, C. Tegenkamp, New J. Phys. 9 (2007) 338.
[48] H. Minoda, T. Shimakura, K. Yagi, F.-J. Meyer zu Heringdorf, M. Horn von Hoegen, Surf. Sci. 432 (1999) 69.
[49] J. Perderau, G.E. Rhead, Surf. Sci. 24 (1971) 555.
[50] R. Hild, C. Seifert, M. Kammler, F.-J. Meyer zu Heringdorf, M. Horn-von-Hoegen, R.A. Zhachuk, B.Z. Olshanetsky, Surf. Sci. 512 (2002) 117.
[51] S.R. Puisto, G. Held, D.A. King, Phys. Rev. Lett. 95 (2005) 036102.

Please cite this article as: M.O. King, et al., The templated growth of a chiral transition metal chalcogenide, Surf. Sci. (2014), http://dx.doi.org/10.1016/j.susc.2014.02.008

[52] M.O. King, I.M. McLeod, D. Hesp, V.R. Dhanak, M. Kadodwala, D.A. MacLaren, Surf. Sci. 606 (2012) 1353.
[53] F. Comin, P. Citrin, P. Eisenberger, J. Rowe, Phys. Rev. B 26 (1982) 7060.
[54] T.Y. Lee, S. Sarbach, K. Kuhnke, K. Kern, Surf. Sci. 600 (2006) 3266.
[55] P. Gambardella, K. Kern, Surf. Sci. 475 (2001) L229.
[56] P. Gambardella, M. Blanc, L. Burgi, K. Kuhnke, K. Kern, Surf. Sci. 449 (2000) 93.
[57] P.C. Dastoor, D.J. O'Connor, D.A. MacLaren, W. Allison, T.C.Q. Noakes, P. Bailey, Surf. Sci. 588 (2005) 101.
[58] C.K. Rhee, C. Jung, B. Ku, J. Solid State Electrochem. 9 (2005) 247.
[59] P. Rodriguez, E. Herrero, A. Aldaz, J.M. Feliu, Langmuir 22 (2006) 10329.
[60] S.M. Driver, D.P. Woodruff, Surf. Sci. 560 (2004) 35.
[61] A.S. Pashinkin, L.M. Pavlova, Inorg. Mater. 41 (2005) 1194.
[62] G. Teeter, Thin Sold Films 515 (2007) 7886.
[63] X. Wu, J. Zhou, A. Duda, Y. Yan, G. Teeter, S. Asher, W.K. Metzger, S. Demtsu, S.H. Wei, R. Noufi, Thin Solid Films 515 (2007) 5798.
[64] Q. Chen, C.W. Lee, D.J. Frankel, N.V. Richardson, PhysChemComm 2 (1999) 41.

Please cite this article as: M.O. King, et al., The templated growth of a chiral transition metal chalcogenide, Surf. Sci. (2014), http://dx.doi.org/10.1016/j.susc.2014.02.008